



# Hot deformation behavior and related microstructure evolution in Au–Sn eutectic multilayers

Yong MAO<sup>1,2,3</sup>, Dan-li ZHU<sup>1,3</sup>, Jun-jie HE<sup>1,2,3</sup>, Chao DENG<sup>4</sup>,  
Ying-jie SUN<sup>1,3</sup>, Guang-jie XUE<sup>1,3</sup>, Heng-fei YU<sup>1,3</sup>, Chen WANG<sup>1,3</sup>

1. School of Materials and Energy, Yunnan University, Kunming 650091, China;
2. School of Physics and Astronomy, Yunnan University, Kunming 650091, China;
3. Materials Genome Institute, Yunnan University, Kunming 650091, China;
4. College of Materials Science and Engineering, Chongqing University, Chongqing 400045, China

Received 5 July 2020; accepted 6 April 2021

**Abstract:** Hot compression was performed on a multilayered Au–20Sn eutectic alloy to investigate the deformation behavior and microstructure evolution. During hot compression, microstructural spheroidization was initiated from plastic instability regions, and it was preferentially activated in vertical lamellae with a growth direction parallel to the compressive direction. Continuous dynamic recrystallization associated with lattice dislocations was the mechanism in both AuSn and Au<sub>5</sub>Sn multilayers. After spheroidization, strain accumulations were weakened in both of the equiaxed phases, and the deformation mechanism was substantially replaced by grain boundary sliding and migration. Based on these findings, hot rolling was conducted on an as-cast Au–20Sn alloy and a foil with a thickness of ~50 μm was successfully prepared. The present study can promote the development of Au–20Sn foils, and provide insights into the deformation behavior and microstructure evolution of multilayered eutectic alloys.

**Key words:** Au–20Sn eutectic alloy; intermetallics; hot compression; multilayered structure; deformation; spheroidization

## 1 Introduction

Research on lead-free solders has been a hot topic in the last decade due to the consideration of environmental and health concerns [1–3]. A large number of lead-free solders, such as Sn–Ag [4], Sn–Zn [5], Sn–In [6] and Au–Sn [7] systems, have been studied extensively as candidates for the replacement of traditional Sn–Pb solder. Among these lead-free solders, Au–20Sn eutectic alloy is widely used in high-power optoelectronics and hermetic sealing applications due to its excellent conductivity, high electromigration and corrosion resistance [8]. However, producing Au–20Sn foils with the desired size (thickness: 30–60 μm) and

properties is still a technological challenge. The microstructure of Au–20Sn eutectic alloy consists of complex structured AuSn and Au<sub>5</sub>Sn intermetallic compounds, which gives rise to the intrinsic brittleness of this alloy at room temperature [9,10].

In recent decades, Au–20Sn foils were commonly prepared using the cascading diffusion and electrodeposition processes [11,12]. However, these two processes both have obvious disadvantages. In the cascading diffusion, the thermodynamic condition in the diffusion process is hard to control, and incomplete alloying usually occurs. Regarding the electrodeposition process, it is costly and unable to support the large-scale production of Au–20Sn preforms. Most importantly,

the lack of precise control of the eutectic composition over a large-scale is the common difficulty of the two processes. Once the composition of the Au–20Sn preform deviates from the eutectic composition point, the melting temperature of the alloy increases sharply, which significantly increases the welding temperature and reduces the welding quality [13,14]. Generally, the effective approaches used to fabricate Au–20Sn preforms are limited, and the development of new manufacturing processes is necessary.

In our earlier study, we found that the as-cast Au–20Sn alloy with fine lamellar colonies showed substantial plasticity during hot compression. This investigation shows that the Au–20Sn alloy may become malleable once the deformation temperature reaches a certain level. Hence, studying the deformation behavior and the microstructure evolution of the Au–20Sn alloy during hot deformation is indispensable. It can help us to understand the plastic behavior and further promote the formability of the alloy.

In this study, hot compression was conducted on the Au–20Sn alloy in a temperature range of 180–240 °C and a strain rate range of 0.001–0.6 s<sup>-1</sup>. The evolution of the microstructure, including the plastic instability of the multilayers, spheroidization process, and deformation behavior after spheroidization were studied systematically. Based on the above findings, a hot rolling experiment was performed on an as-cast Au–20Sn alloy, and a foil with a thickness of ~50 μm was successfully prepared. The present study can promote the development of Au–20Sn alloy foils and provide insights into the deformation behavior of multilayered eutectic alloys.

## 2 Experimental

### 2.1 Preparation of as-cast Au–20Sn alloy

The Au–20Sn master alloy was prepared in an electromagnetic induction furnace in vacuum by melting a pure gold sheet (99.999% pure) and tin particles (99.99% pure) in a graphite crucible. The master alloy was then heat-treated at 350 °C for 10 min and cast to prepare rod-like specimens with the dimensions of 5 mm × 5 mm × 50 mm by employing a graphite mould. A satisfactory surface quality of the as-cast specimens was obtained due to the excellent fluidity of the alloy at the heated

temperature.

Additionally, an Au–20Sn ingot with dimensions of 20 mm (length) × 20 mm (width) × 4 mm (thickness) was prepared by employing a flat mold for the rolling process.

### 2.2 Hot compression

Samples with dimensions of 5 mm × 5 mm × 7 mm (height) were machined from the as-cast rod-like specimens for hot compression experiments. The hot compression tests were performed using an ETM205D electronic universal testing machine equipped with a high-temperature furnace. During hot compression, the temperatures were set as 180, 200, 220 and 240 °C, and the strain rates were 0.001, 0.1 and 0.6 s<sup>-1</sup>, respectively, to systematically study the influence of temperature and strain rate on the microstructure evolution and deformation behavior. The accuracies of the electronic universal testing machine and the high-temperature furnace are ±0.5% and ±1.5 °C, respectively. Before compression, the samples were held in the furnace for 5 min to ensure that they reached the testing temperature. After compression, the samples were water quenched immediately to reserve the deformation structures.

### 2.3 Characterization

To clarify the microstructure evolution and deformation behavior during hot deformation, samples subjected to 20%, 60%, 120% and 200% compressive strains were analyzed. The samples used for microstructure observations were cut from the compressive direction–transverse direction (CD–TD) section and then prepared by a metallographic technique without etching. The backscattered electron (BSE) images were obtained by using a field emission scanning electron microscopy (FESEM, JEOL-JSM 7800F) system equipped with an energy-dispersive X-ray spectroscopy (EDS). The electron backscatter diffraction (EBSD) data were collected using an EBSD camera (HKL Channel 5 System installed on JEOL-JSM 7800F, Cambridge, MA). The samples used for EBSD measurements were prepared by argon ion polishing (Gatan Iliion II 697) to obtain a high-quality surface without residual stress.

### 2.4 Rolling

Based on the findings from the hot

compression process, a tentative hot rolling experiment was performed on an as-cast Au–20Sn alloy. The rolling process was performed at 220 °C with a linear speed of 1 m/min and a pass reduction of 15%–20%. The principles used to select these parameters are discussed in detail in the Section 4.4. The rollers of the machine used in this study were heated to a given temperature to prevent the loss of heat (rollers were equipped with a resistive heater and a temperature measuring device). The temperature fluctuation during the hot rolling process was about  $\pm 3$  °C, which was considered an acceptable error range.

### 3 Results

#### 3.1 Nanolayered structure of as-cast Au–20Sn alloy

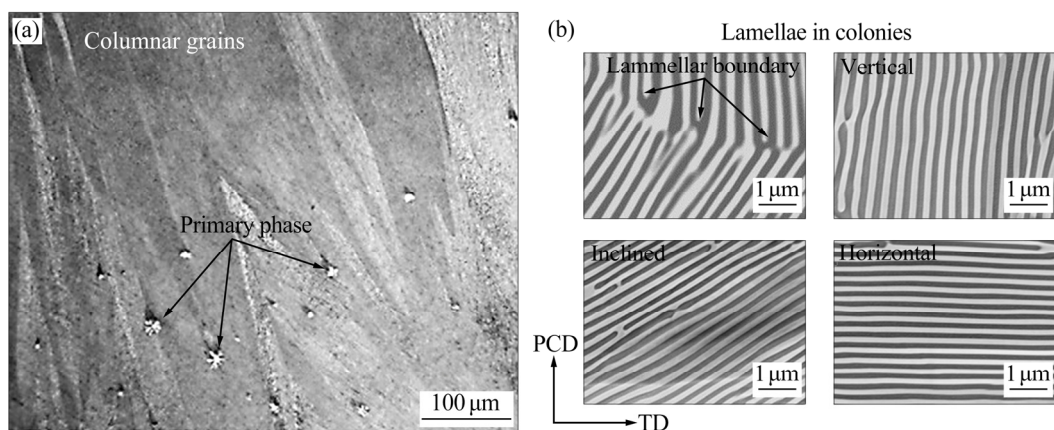
Figure 1(a) shows that the as-cast Au–20Sn eutectic alloy is composed of coarse columnar grains with a width of 20–150  $\mu\text{m}$ , and plum blossom-like and punctiform particles with a size of 3–10  $\mu\text{m}$  are randomly embedded in the coarse columnar grains. EDS confirms that these particles are the  $\text{Au}_5\text{Sn}$  primary phase. The high-magnification BSE images in Fig. 1(b) reveal that these columnar grains comprise a typical lamellar eutectic structure. The phases with dark and bright contrast regions are identified as AuSn and  $\text{Au}_5\text{Sn}$  intermetallic compounds in the high-resolution BSE images based on their distinct compositions. Phase identification can further refer to our previous TEM characterization and Au–Sn phase diagram [15,16]. Additionally, the eutectic colonies show random lamellar growth directions that can be classified

into vertical, inclined, and horizontal lamellae according to the potential compressive direction (PCD). The lamellar boundary between the colonies is not straight, and many structural defects, such as disconnections and misconnections, are introduced at these locations, leading to the formation of disordered microstructures near the lamellar boundary. The measurements of lamellar thickness in the colonies with different growth directions indicate that there is no significant difference in the lamellar thicknesses of these colonies, and the average lamellar thickness of the AuSn and  $\text{Au}_5\text{Sn}$  layers can be given as  $\sim 107$  nm and  $\sim 132$  nm, respectively.

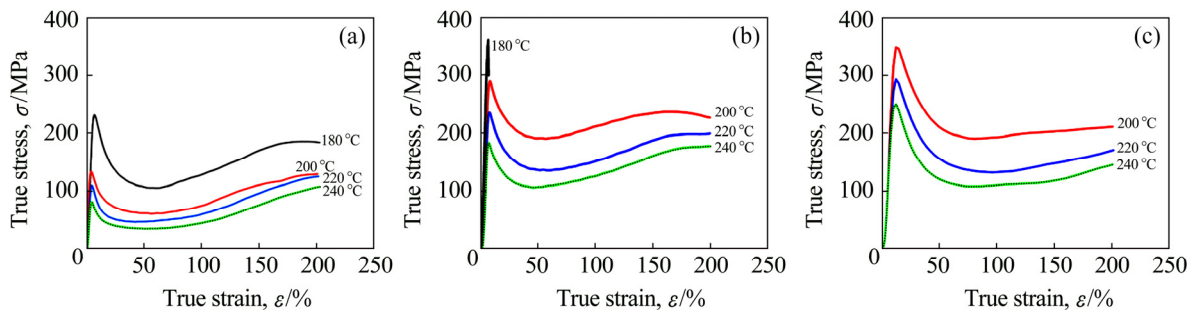
#### 3.2 Hot compression behavior

Figure 2 shows the flow curves of Au–20Sn alloys subjected to hot compression at various temperatures (from 180 to 240 °C) and different strain rates (from 0.001 to  $0.6\text{ s}^{-1}$ ). Under these conditions, all the curves exhibit a stress peak during initial deformation and then drop rapidly because of strain softening caused by the dynamic recrystallization process (DRX) [17]. It can be seen that the peak stress is significantly influenced by the temperature and the strain rate, which monotonously increases with the decreasing temperature or increasing strain rate. At the lowest strain rate of  $0.001\text{ s}^{-1}$ , the samples are successfully deformed at 200% strain without failure in the temperature range from 180 to 240 °C, as shown in Fig. 3. Nevertheless, serious wrinkles can be seen at the edge of the sample deformed at 180 °C.

According to Fig. 2(a), the peak stress of the sample deformed at 180 °C is twice as high as that



**Fig. 1** Microstructure of as-cast Au–20Sn eutectic alloy: (a) Optical micrograph showing coarse columnar grains in alloy; (b) Columnar colonies exhibiting lamellar structure with different growth directions



**Fig. 2** Flow curves of Au–20Sn alloys subjected to hot compression from 180 °C to 240 °C at different strain rates: (a)  $0.001 \text{ s}^{-1}$ ; (b)  $0.1 \text{ s}^{-1}$ ; (c)  $0.6 \text{ s}^{-1}$

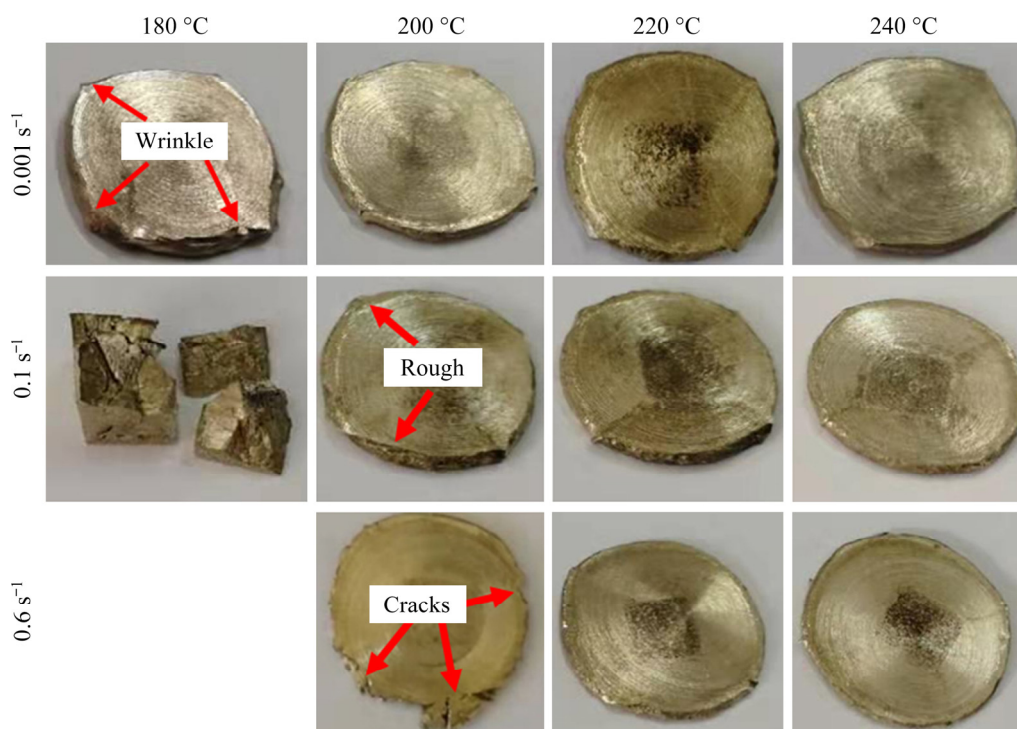


**Fig. 3** Au–20Sn samples after hot compression

of the sample deformed at 200 °C, and the rheological resistance is also much higher than that of the samples deformed at higher temperatures. The presence of serious wrinkles indicates that uneven deformation behavior occurs in the sample deformed at 180 °C. Regarding the Au–20Sn alloys with a nanolayered microstructure subjected to hot deformation, strain softening caused by DRX is closely related to deformation temperature. A low deformation temperature leads to localized strain concentration because the strain softening is inhibited, and uneven deformation behaviors, such as wrinkles, are introduced in the sample. In the compression process, 180 °C may be the minimum temperature for alloy forming at the strain rate of

$0.001 \text{ s}^{-1}$ . When the strain rate increases to  $0.1 \text{ s}^{-1}$ , brittle fracture occurs directly at the initial stage in deformation at 180 °C, and plastic deformation behavior can hardly occur in this condition due to the absence of strain softening. When the deformation temperature increases to 200 °C, the Au–20Sn alloy can be successfully deformed at 200% strain, but the edge of the deformed sample is rather rough. With increasing temperatures to 220 and 240 °C, the surface qualities of the deformed samples are improved significantly. When the strain rate further increases to  $0.6 \text{ s}^{-1}$ , the appropriate temperature for alloy forming increases. Edge cracks are intensely introduced, even to the sample deformed at 200 °C, and satisfactory surface-quality

can only be obtained when the deformation temperature exceeds 220 °C. Clearly, besides the temperature, the formation of macroscopic defects during hot compression is related to the strain rate. At a given deformation temperature, a higher strain rate leads to more pronounced strain hardening (indicated by the much higher flow stress in Fig. 2), and a higher temperature is needed to achieve dynamic recovery, diffusion and recrystallization to suppress the localized strain concentration [18]. Overall, the formability of the Au–20Sn alloy is extremely sensitive to both the temperature and strain rate, these two parameters should be fully considered when formulating a hot forming process for this alloy.

### 3.3 Microstructure evolution

Figure 4 shows the microstructures of the Au–20Sn alloy deformed at 220 °C and 0.1 s<sup>-1</sup> with strains of 20% and 60%. Considering that the

lamellar growth directions of the colonies are diverse, the analyses of microstructures focus on the locations that consist of colonies with different representative growth directions. For the sample with 20% compressive strain, spheroidization develops substantially in the vertical lamellae, while this phenomenon is hard to observe in the inclined and horizontal lamellae. Regarding the colonies with vertical lamellae, plastic instability, such as severe bending and “S” shear, can be seen clearly in the remaining lamellae. Additionally, little shear is also observed in the inclined lamellae, and spheroidized structures are gradually introduced in these sheared regions, as denoted in Fig. 4(a<sub>3</sub>). As the compressive strain increases to 60%, severe bending and “S” shear become more pronounced in the inclined and horizontal lamellae. Simultaneously, spheroidization in the inclined and horizontal lamellae develops, which is gradually accompanied by the introduction of more plastic

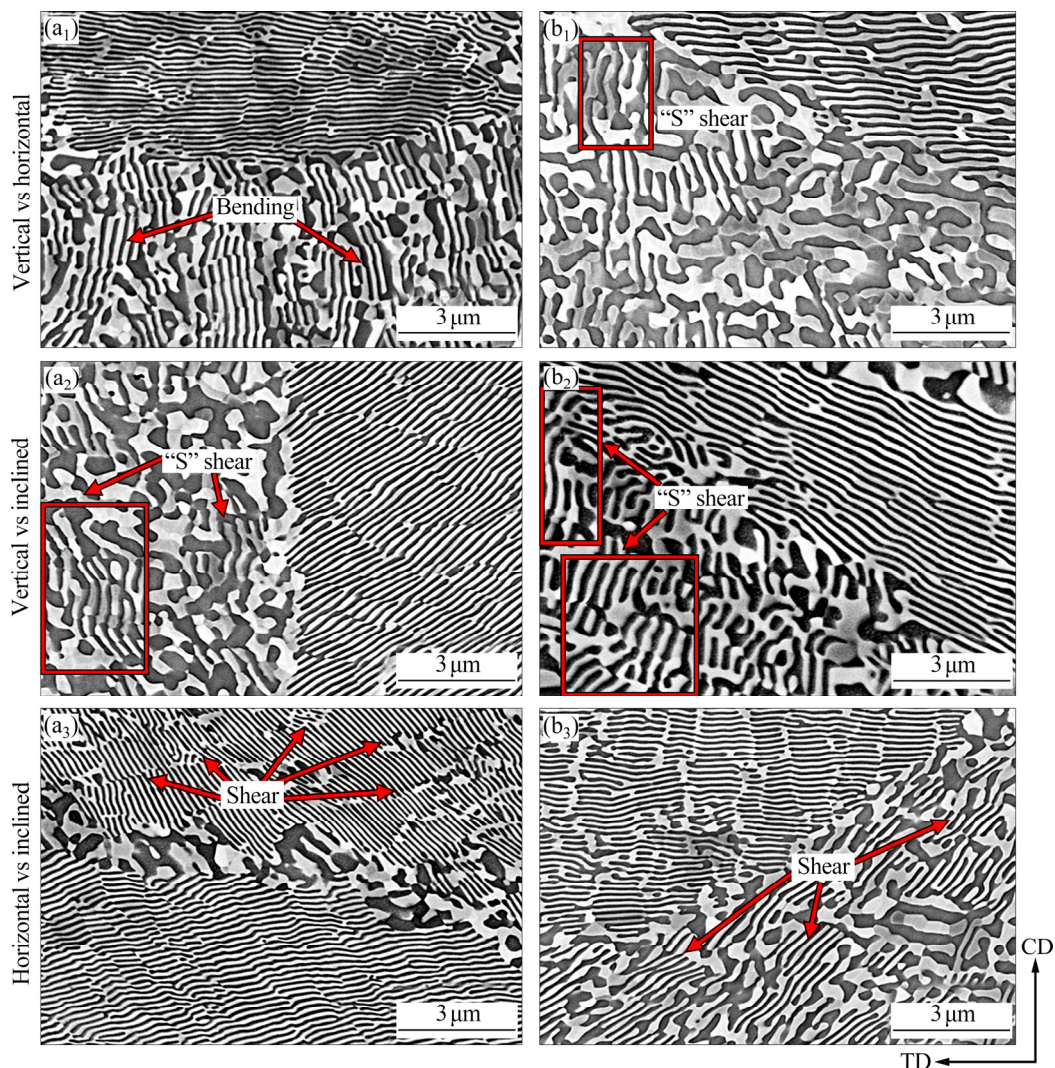


**Fig. 4** Microstructures of Au–20Sn alloys deformed at 220 °C and 0.1 s<sup>-1</sup> to strain of  $\epsilon=20\%$  (a<sub>1</sub>–a<sub>3</sub>) and  $\epsilon=60\%$  (b<sub>1</sub>–b<sub>3</sub>)

instability regions. However, the spheroidization rates in these two colonies are much lower than those in the vertical lamellae. The spheroidization rates in the colonies of the Au–20Sn alloy are in the following order: vertical > inclined > horizontal.

As the compressive strain increases to 120%, microstructural spheroidization becomes more pronounced, and abundant equiaxed AuSn and Au<sub>5</sub>Sn phases can be seen. In spite of this, quite a large fraction of phases still maintain a lamellar structure morphology, as seen in Fig. 5(a<sub>1</sub>). Note that the vertical lamellae have been almost exhausted under such a strain condition, and microstructural spheroidization in the inclined lamellae becomes more intense. Generally, the closer the growth direction of the inclined colonies is to the vertical colony, the more easily the spheroidization can occur. However, there are still numerous horizontal or sub-horizontal lamellae remaining in the sample, as shown in Fig. 5(a<sub>3</sub>). When the compressive strain further increases to 200%, the majority of the microstructure has completed the spheroidization process. AuSn and Au<sub>5</sub>Sn phases in the sample become more equiaxed, and their phase sizes become larger than those with a strain of 120%. Nevertheless, some horizontal lamellae can still be observed in the sample, and the size of the equiaxed phases near these horizontal lamellae is much smaller than the phases elsewhere, as shown in Fig. 5(b<sub>3</sub>). Evidently, it is further confirmed that the spheroidization rates of the colonies are rather different, which is strongly affected by the initial lamellar growth direction.

## 4 Discussion

### 4.1 Deformation behavior and spheroidization in multilayers

The Au–20Sn alloy shows intrinsic brittleness at room temperature because its microstructure consists of two brittle intermetallic compounds. However, the study has confirmed that this alloy shows superplasticity when the deformation temperature increases to 220 °C. Before spheroidization, deformation behaviors, such as bending and shear, can be observed clearly in the multilayers. When the alloy is subjected to hot compression, the plastic flow takes place in the AuSn and Au<sub>5</sub>Sn layers to coordinate strain. Under such a mechanical model, bending instability is more likely to be primitively introduced in the vertical lamellae because the lamellar growth direction is exactly parallel to the compressive stress direction. With the increase in compressive strain, plastic flow in terms of bending in the two phases becomes more and more intense, and shears across the multilayers can be subsequently introduced, as shown in Fig. 6(a). Localized shear can lead to the effective initiation of spheroidized structures according to the microstructure evolution. The distribution density of shear instability regions in the vertical lamellae will increase rapidly as the compressive strain further increases, leading to the formation of a knobby structure. Spheroidization then develops intensely based on this densely distributed shear and spreads

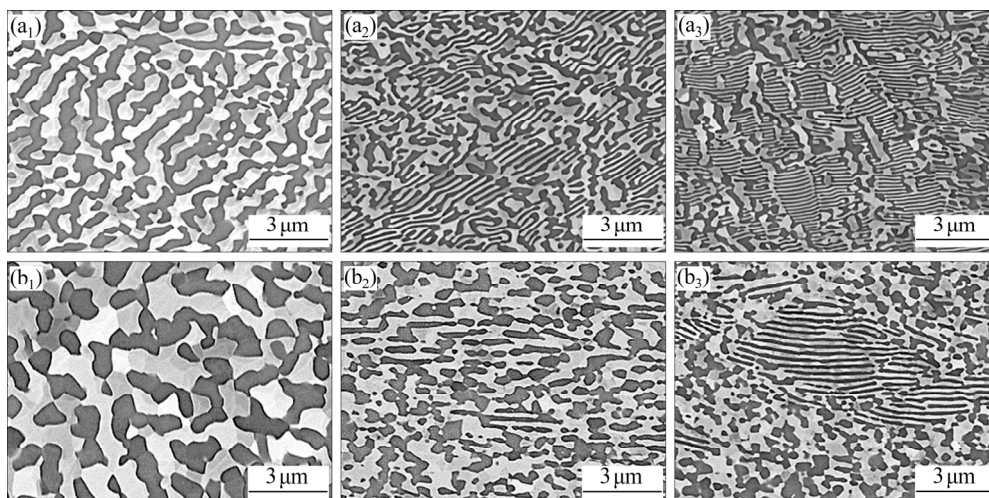


**Fig. 5** Microstructures of samples subjected to different compressive strains of  $\varepsilon=120\%$  (a<sub>1</sub>–a<sub>3</sub>) and  $\varepsilon=200\%$  (b<sub>1</sub>–b<sub>3</sub>): (a<sub>1</sub>) Spheroidized structure; (a<sub>2</sub>) Remained inclined structure; (a<sub>3</sub>) Remained horizontal or sub-horizontal lamellae; (b<sub>1</sub>) Completely equiaxed structure, (b<sub>2</sub>) Spheroidized structure with lamellar structure; (b<sub>3</sub>) Remained horizontal lamellae

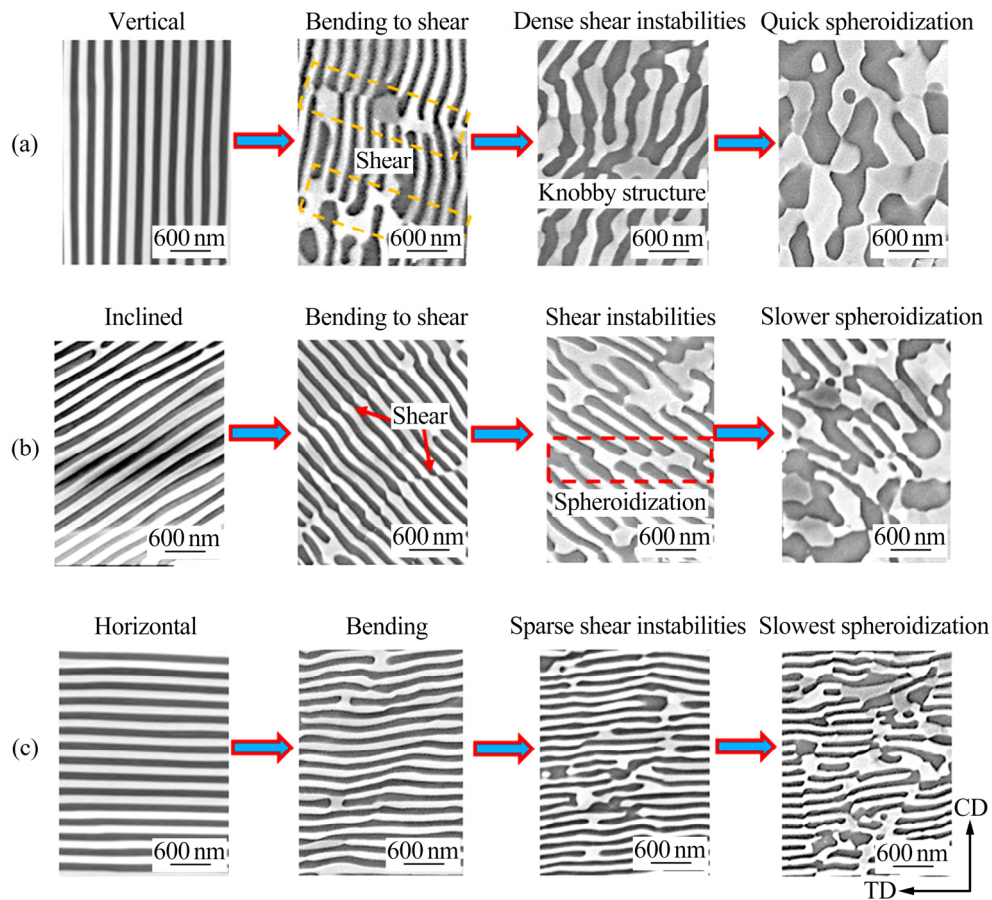


**Fig. 6** Comparison of spheroidization processes in colonies with different lamellar growth directions: (a) Vertical lamellae; (b) Inclined lamellae; (c) Horizontal lamellae

rapidly in the colonies with vertical lamellae. As a result, a complete equiaxed microstructure can be introduced soon in these colonies. While for the colonies with inclined lamellae, the formation of bending and shear across the multilayers will slow due to the deviation angle between the lamellar growth direction and the compressive stress direction. The slower development of plastic instability regions leads to a slower spheroidization process in these colonies, as shown in Fig. 6(b). For the horizontal lamellae, compressive stress can also cause bending across the multilayers, but the radius of the bent lamellae is smooth and these bending instability regions can hardly transform into severe shear instability regions, as seen in Fig. 6(c). As a result, the colonies with horizontal lamellae show the lowest spheroidization rate during the hot compression process.

It is clear that the plastic behavior of the eutectic multilayers during hot compression is sensitive to the initial lamellar growth directions, and plasticity can be mediated by plastic instability.

However, the distribution of localized shears is unable to steadily release the compressive strain, which will lead to local fracture during subsequent deformation [19]. Whereas for this alloy subjected to hot deformation, localized shear can be further mediated by spheroidization. The internal mechanism responsible for spheroidization favoring the shear instability needs to be clarified to further understand the microstructure evolution of the multilayers.

To explain this issue, EBSD is performed on the vertical lamellae that have been subjected to intense “S” shear, as shown in Fig. 7(a), where the dark and bright contrast regions are the AuSn and Au<sub>5</sub>Sn phases. As shown in the band contrast map, numerous grain boundaries (>2°, GBs) gradually develop in both AuSn and Au<sub>5</sub>Sn layers, with the formation of some equiaxed grains. Meanwhile, some GBs still appear discontinuous, and it can be predicted that spheroidization will take place here soon. Note that both the equiaxed phases and the GBs are all located near the shear instability regions.

The misorientations that accumulated in two deformed AuSn layers and two deformed Au<sub>5</sub>Sn layers are shown in Fig. 8. The typical point-to-origin misorientations parallel and vertical to the initial lamellar growth direction are analyzed near the newly developed grain boundaries. The results

indicate that misorientations along the arrows A1, B1, C1 and D1 (along the initial lamellar growth direction) of the layers show the considerable misorientation accumulation, while misorientations along the arrows A2, B2, C2 and D2 (vertical to the initial lamellar growth direction) are barely changed.

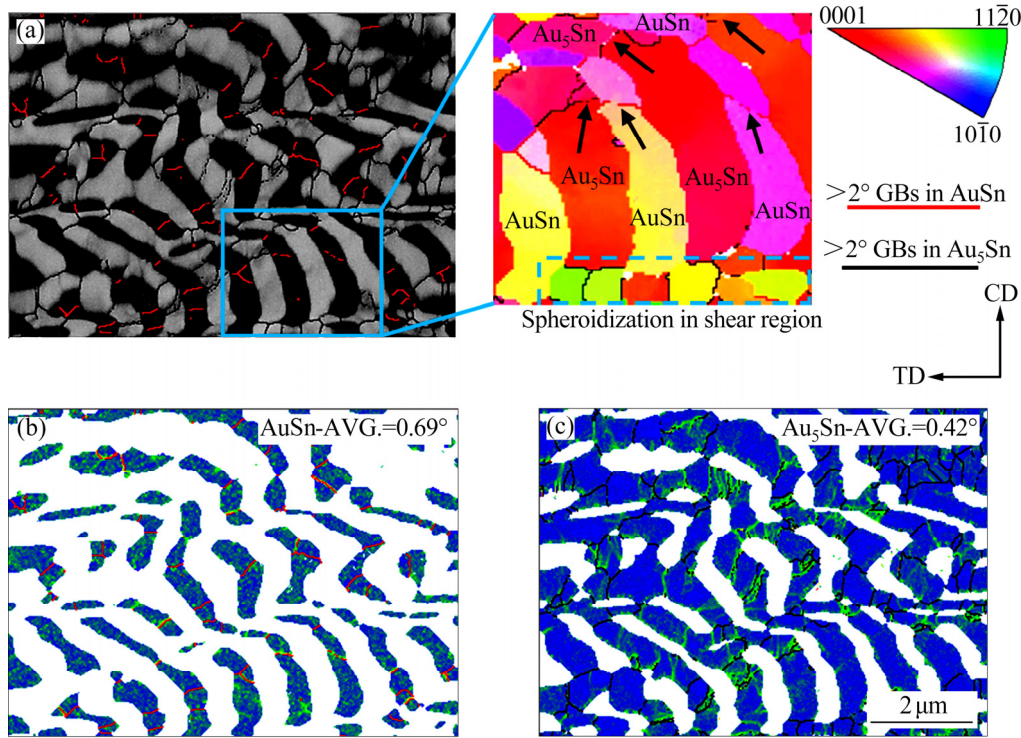


**Fig. 7** EBSD performed on deformed vertical multilayers in sample subjected to strain of 20% at 220 °C and 0.1 s<sup>-1</sup>: (a) Band contrast map and GBs development in AuSn and Au<sub>5</sub>Sn layers; (b–c) KAM distributions in deformed AuSn and Au<sub>5</sub>Sn layers

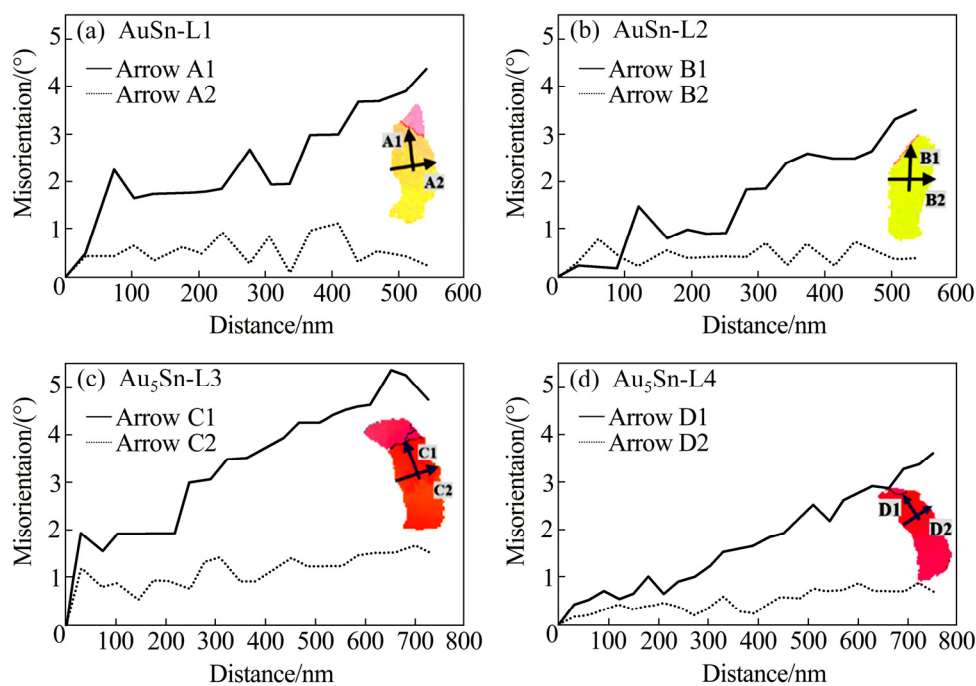


**Fig. 8** Misorientations accumulated in deformed AuSn and Au<sub>5</sub>Sn layers (L–Lamellae)

Such misorientation accumulation in AuSn and Au<sub>5</sub>Sn layers indicates that strain accumulation is more likely to distribute from the layer interior to the shear instability regions. The above findings suggest that the development of GBs in sheared regions is based on a gradual increase in the number of misorientations by the continuous absorption of dislocations in sub-GBs during straining, and this phenomenon is related to continuous dynamic recrystallization (CDRX) [20,21]. Kernel average misorientation (KAM) maps of the deformed AuSn and Au<sub>5</sub>Sn phases shown in Figs. 7(b, c) can further confirm this mechanism. KAM can be interpreted in terms of the density of geometrically necessary dislocations to give local strain value. A higher KAM value means more strain accumulation [22,23]. Clearly, the shear instability regions in the two phases extremely favor the strain accumulation, which can provide sufficient energy for the formation and development of GBs. Thus, the spheroidization process in the nanolayered Au–20Sn alloy during hot compression is primarily based on CDRX in the shear instability regions. Additionally, strain accumulation in the AuSn phase seems to spread from the shear instability regions to the lamellar interior, but the majority of strain that accumulates in the Au<sub>5</sub>Sn phase seems to be intensively distributed only near the shears. This phenomenon suggests that strain transfer is much easier in the AuSn matrix than that in the Au<sub>5</sub>Sn phase. Furthermore, the average KAM value in the AuSn phase is higher than that in the Au<sub>5</sub>Sn phase, even though they are subjected to the same compressive stress condition, indicating that the strain accumulation ability of the AuSn layer is much better than that of the Au<sub>5</sub>Sn layer. The

different deformation abilities in the two phases are probably attributed to their different crystal structures. This may be the same reason why the degree of microstructural spheroidization in the AuSn phase is more pronounced, with more equiaxed grains observed in the AuSn KAM map, as shown in Fig. 7 (b).

#### 4.2 Deformation behaviors in equiaxed microstructure

Microstructural spheroidization is a continuous process in the Au–20Sn alloy during hot compression, and its activity even lasted during the high-strain stage at strain of 200%. Nevertheless, the majority of the lamellae have transformed into equiaxed grains before being subjected to this strain condition, although a few horizontal lamellae with slow spheroidization rates still remain. The equiaxed microstructure has gradually become the primary carrier of compressive strain, and especially plays a dominant role in the latter compression process. Hence, study of deformation behaviors on the equiaxed microstructure is necessary.

Figure 9(a) shows the equiaxed microstructure of the sample subjected to strain of 200% at 220 °C and 0.1 s<sup>-1</sup>. Misorientation analyses indicate that complete recrystallization has occurred in both AuSn and Au<sub>5</sub>Sn phases. Such a microstructure can represent the general microstructure condition of this sample, according to the microstructure evolution in Fig. 5. The average grain sizes of the equiaxed AuSn and Au<sub>5</sub>Sn phases in this sample are ~343.6 and ~452.7 nm, respectively. The separated microstructures of the two phases in terms of KAM maps are shown in Figs. 9(b, c),

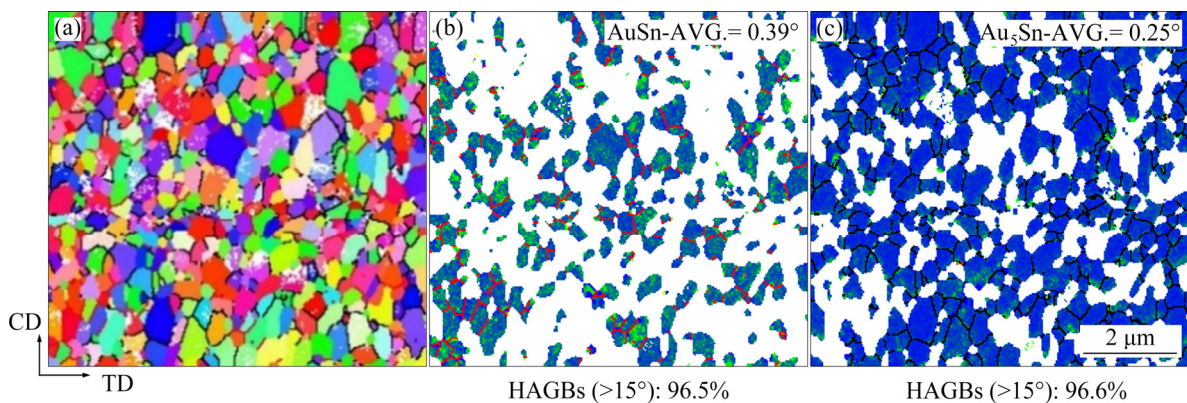


**Fig. 9** EBSD performed on equiaxed microstructure in sample subjected to strain of 200% at 220 °C and 0.1 s<sup>-1</sup>: (a) IPF map of AuSn and Au<sub>5</sub>Sn phases; (b, c) KAM distributions in deformed AuSn and Au<sub>5</sub>Sn equiaxed grains, respectively

and the average KAM values are calculated to be  $0.39^\circ$  and  $0.25^\circ$ , which are obviously lower than those in the lamellar structures.

Similar to the previous study on layers, two AuSn grains and two Au<sub>5</sub>Sn grains are randomly selected to investigate the in-grain misorientation accumulations, as shown in Fig. 10. However, the misorientations parallel and vertical to the grain boundary in the four grains oscillate up and down but are all below  $0.7^\circ$ , which means that few misorientations accumulate inside both the equiaxed AuSn and Au<sub>5</sub>Sn grains. These phenomena confirm that strain accumulation based on the lattice dislocations decreases significantly after the lamellae transformed into the equiaxed structure. This implies that the plastic deformation mechanism that mediates compressive strain may have changed from dislocation slip to another mechanism in the equiaxed phases.

To further investigate the deformation behavior of the equiaxed microstructure, EBSD is also conducted on the sample subjected to strain of 200% at  $220^\circ\text{C}$  and  $0.001\text{ s}^{-1}$ , as shown in Fig. 11. Similarly, misorientations also cannot accumulate

effectively in the equiaxed phases; the number of accumulated in-grain misorientations is even less than that in the sample deformed at the strain rate of  $0.1\text{ s}^{-1}$ , as determined by comparing the misorientation-distance curves. Figures 11(b, c) show that the ability of strain to accumulate (evaluated by the average KAM value) based on the lattice dislocations in this sample is also inferior to that in the sample deformed at  $0.1\text{ s}^{-1}$ . Additionally, it is noted that the average grain sizes of the equiaxed AuSn and Au<sub>5</sub>Sn phases in this sample are  $\sim 776.3$  and  $\sim 984.2$  nm, respectively, which are approximately 2.2 times larger than those in the sample deformed at  $0.1\text{ s}^{-1}$ . Because grain boundary sliding and migration are sensitive to the strain rate, the introduction of a larger grain size in hot deformation at a lower strain rate is usually attributed to these deformation mechanisms, as reported in many studies [24–26]. Besides, grain boundary bulging is observed in the two deformed samples in Figs. 9 and 11 (seen in the KAM maps), which further confirms the occurrence of grain boundary sliding and migration in the equiaxed AuSn and Au<sub>5</sub>Sn phases. Thus, it can be

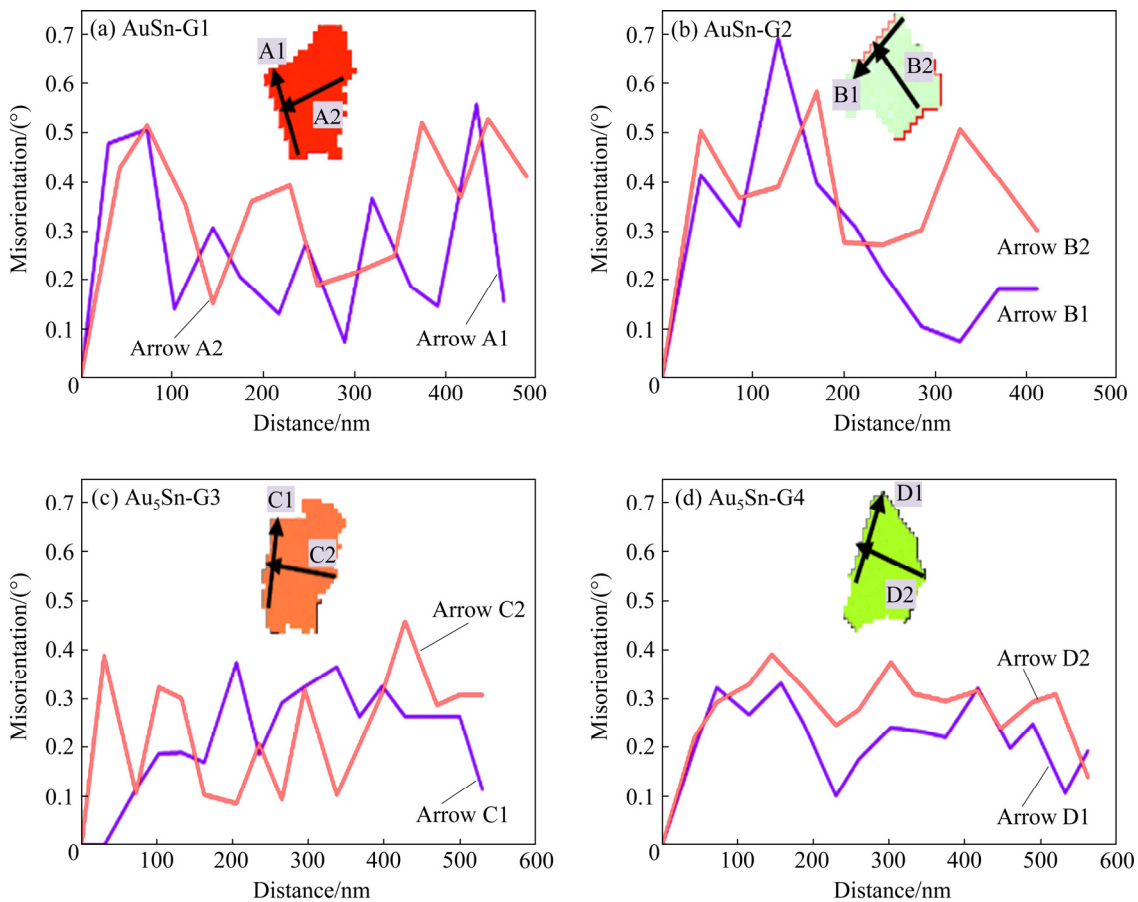


**Fig. 10** Misorientations accumulated in deformed AuSn and Au<sub>5</sub>Sn equiaxed grains (G–Grain)

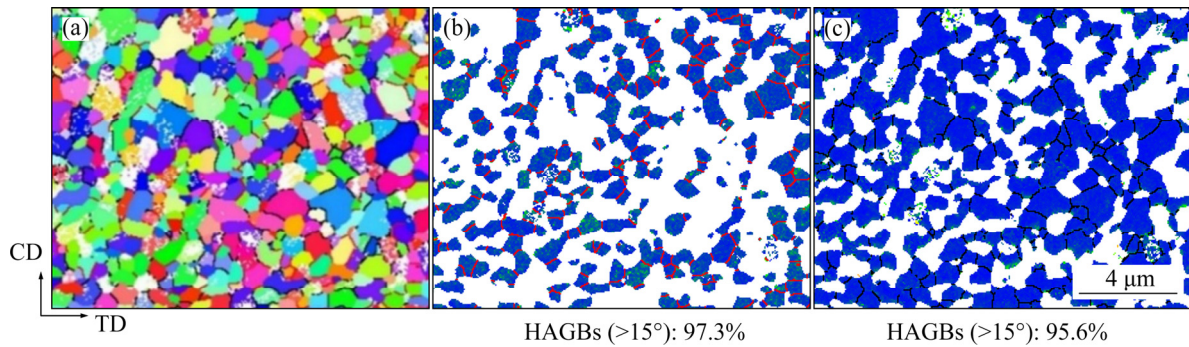


**Fig. 11** EBSD performed on equiaxed microstructure of sample subjected to strain of 200% at 220 °C and  $0.001 \text{ s}^{-1}$ : (a) IPF map of AuSn and Au<sub>5</sub>Sn phases; (b,c) KAM distributions in deformed AuSn and Au<sub>5</sub>Sn equiaxed grains, respectively

preliminarily concluded that grain boundary sliding and migration have become important deformation mechanisms that coordinate compressive strain after the multilayers is transformed into equiaxed grains, which leads to a rapid decrease in the extent of strain accumulation caused by the declining dislocation slip activity. The contribution of grain boundary sliding and migration to the strain coordination will be enhanced as the strain rate decreases.

#### 4.3 Transition of deformation mechanisms

Regarding the Au–20Sn alloy during hot deformation, microstructure evolution is intricate due to the presence of two complicated structured intermetallic compounds (AuSn+Au<sub>5</sub>Sn). The investigations on the deformation mechanisms of the two phases during hot compression are important because these mechanisms have a significant influence on microstructure evolution. As mentioned previously, CDRX, in terms of lattice dislocations, occurs intensely in both the AuSn and Au<sub>5</sub>Sn layers, suggesting that slip occurs in these two lamellar phases. For the hexagonal-structure materials, analysis of the in-grain misorientation axis (IGMA) distribution is an effective method to identify what kinds of dislocations are activated in a deformed microstructure [27,28]. Figure 12(a) shows the IGMA analysis of the deformed AuSn layers. It shows that the IGMA is mostly along the  $\langle 0001 \rangle$  direction, which suggests that lattice rotation of the matrix is primarily based on the *c*-axis and this grain reorientation behavior can directly correspond to prismatic  $\langle a \rangle$  slip [27]. It is well known that the *c/a* ratio usually plays a crucial role

in influencing the selection of the deformation mechanisms in hexagonal-structure alloys [29,30]. It is reported that the dominant deformation mechanism in the hexagonal-structure metals, such as Mg (*c/a*: 1.623) and Zn (*c/a*: 1.856) alloys with a higher *c/a* value, is basal  $\langle a \rangle$  slip, while the prismatic  $\langle a \rangle$  slip is the dominant mechanism in Zr (*c/a*: 1.592) and Ti (*c/a*: 1.588) alloys with a lower *c/a* ratio [31–34]. As the *c/a* ratio of the AuSn phase with a double HCP crystal structure is only 1.278,  $\{10\bar{1}0\}$  prismatic planes are the most close-packed planes and the slip direction is likely to be the  $\langle 11\bar{2}0 \rangle$  direction, according to the crystal structure parameters in Fig. 12(b). Thus, it can be concluded that prismatic  $\langle a \rangle$  slip is the dominant deformation mechanism in the AuSn layers during the hot compression. Regarding the deformed Au<sub>5</sub>Sn layers, the IGMA is mostly along the  $\langle 10\bar{1}0 \rangle$ . Such an IGMA distribution can correspond to basal  $\langle a \rangle$  or pyramidal  $\langle c+a \rangle$  slip activities in hexagonal-structure alloys [35]. Figure 12(d) shows the crystal structure of the Au<sub>5</sub>Sn phase, which possesses a trigonal structure. Because a majority of the crystal planes of the Au<sub>5</sub>Sn phase exhibit 60° rotational symmetry (six-fold symmetric axis) about the *c*-axis, the trigonal structure ( $a=b \neq c$ ,  $\alpha=\beta=90^\circ$ , and  $\gamma=120^\circ$ ) can be transformed to a hexagonal structure. Note that the primary slip systems and their activities in the trigonal structure are in full accord with those in the hexagonal structure; discussions on the deformation mechanisms of the Au<sub>5</sub>Sn phase made based on the hexagonal-structure alloys are fully applicable. Evidently, from crystallographic theory, the basal  $\langle a \rangle$  slip system probably activates easily in the Au<sub>5</sub>Sn phase owing

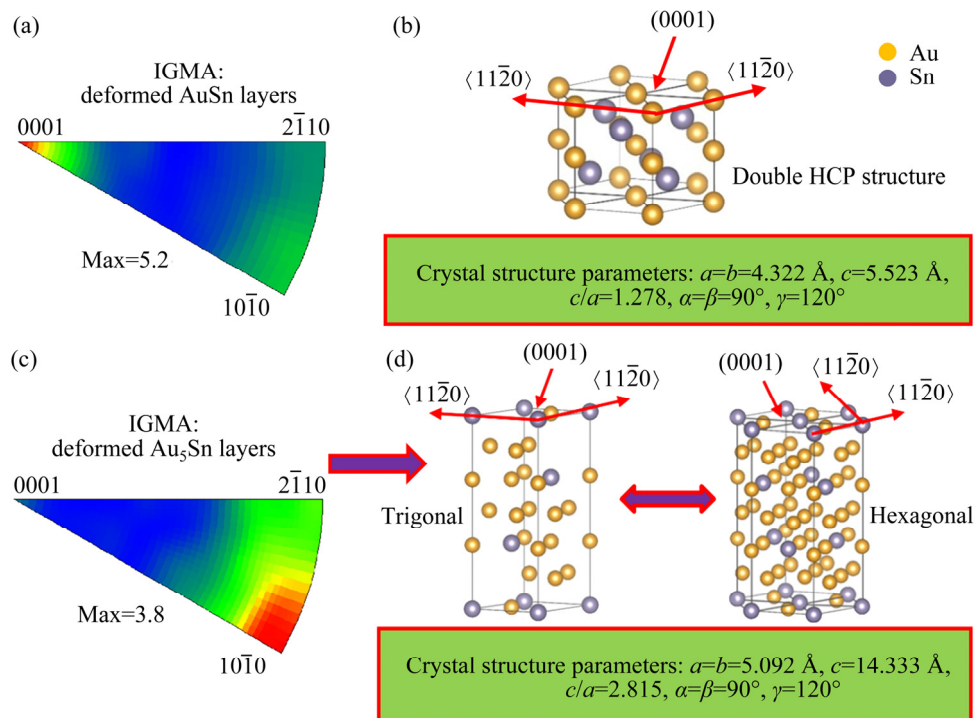


**Fig. 12** Deformation mechanisms of AuSn and Au<sub>5</sub>Sn layers: (a) IGMA of deformed AuSn layers; (b) Crystal structure parameters of AuSn intermetallic compound; (c) IGMA of deformed Au<sub>5</sub>Sn layers; (d) Crystal structure parameters of Au<sub>5</sub>Sn intermetallic compound (The IGMA analysis is based on the deformed multilayers in Fig. 7(a))

to its high  $c/a$  ratio and complicated crystal structure. Combined with the IGMA result, basal  $\langle a \rangle$  slip is the dominant deformation mechanism in the Au<sub>5</sub>Sn layers during hot compression. Additionally, it is now clear that the difference in the strain accumulation abilities of the two phases is closely related to their crystal structures, and the higher crystal symmetry of the AuSn phase can give rise to a better deformability and thus more strain accumulation.

However, after the spheroidization process, accumulated strain in terms of lattice dislocations is significantly weakened in both the equiaxed AuSn and Au<sub>5</sub>Sn phases. The IGMA analyses of the two equiaxed phases shown in Figs. 13(a, c) can further confirm this finding because the intensities of the preferred distribution of IGMA in the two phases are all reduced significantly. Combined with the previous analyses, dislocation slip has been substantially replaced by grain boundary sliding and migration. The transition of the deformation mechanism in this alloy during hot deformation can be rationalized by the following aspects. For the lamellar structure, the phase boundary is the unique interface between the lamellae, and GB sliding and

migration cannot occur because of the lack of effective GBs. As a consequence, only the dislocation slip activity can be selected to mediate deformation strain. For the equiaxed structure, the number of effective GBs increases rapidly, and GB sliding and migration can take place subsequently. With the increasing fraction of the spheroidized structure, GB sliding and migration become important deformation mechanisms owing to the presence of a considerable fraction of effective GBs and high temperature. Additionally, the vast majority of the GBs introduced by the CDRX process are HAGBs according to Fig. 9(b) and Fig. 11(b). The high average misorientation of the GBs in the samples can effectively support GB sliding and migration [36]. As a result, the contribution of slip activity on the strain coordination will be weakened in the two equiaxed phases. Deformation strain in the equiaxed microstructures, which is primarily mediated by GB sliding and migration gives rise to the relatively random grain distribution of the two equiaxed phases, and no obvious deformation texture is introduced in the sample with a large strain of 200%, according to Figs. 13(b, d).

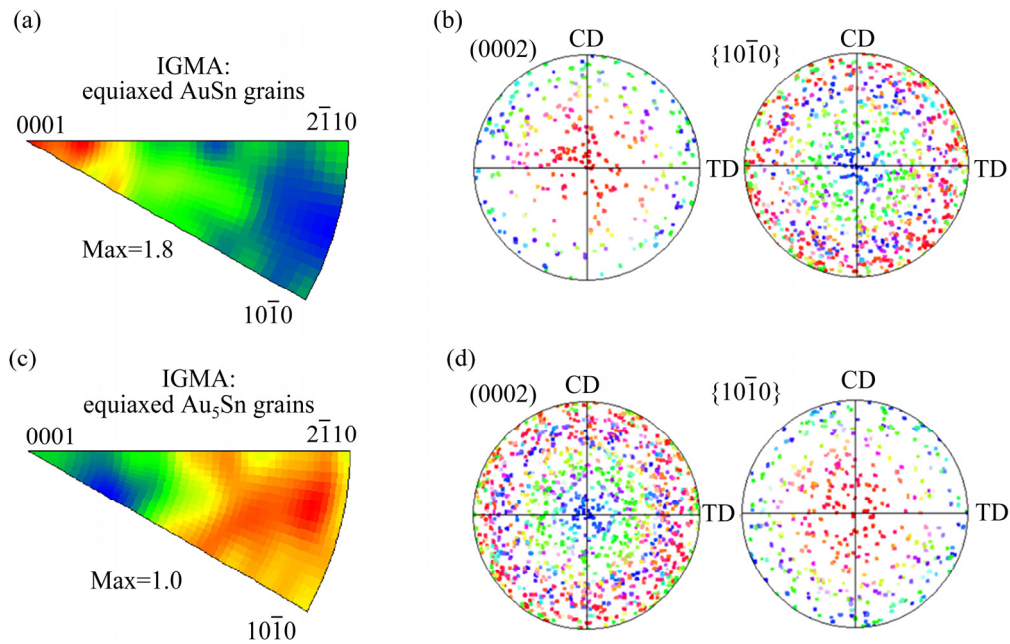


**Fig. 13** Deformation mechanisms and texture of equiaxed microstructure: (a) IGMA analysis of equiaxed AuSn grains; (b) Orientation distribution of equiaxed AuSn phase; (c) IGMA analysis of equiaxed Au<sub>5</sub>Sn grains; (d) Orientation distribution of equiaxed Au<sub>5</sub>Sn phase (The IGMA and texture analyses are based on the equiaxed microstructure in Fig. 9(a))

Although the primary deformation mechanisms of the alloy during hot compression are discussed, further issues still exist. For example, what is the dislocation slip mode in terms of atomic scale? The dislocation slip mode of the AuSn and Au<sub>5</sub>Sn phases may be achieved between Au and Au atoms, Sn and Sn atoms or Au and Sn atoms according to the crystal structures of the two phases. However, at present, we have no idea which mode is reasonable and has actually been activated during the dislocation slip process. Further studies can focus on more deeply investigating the deformation mechanism of the two phases by combining HRTEM and first-principle calculation methods, but this will be challenging because of the extremely complicated crystal structures of the two intermetallic compounds.

#### 4.4 Exploration of manufacturing process of Au–20Sn foil

The processes currently used to fabricate Au–20Sn foil that meets industry requirements have all abandoned the plastic working methods because of the presence of the two brittle phases of AuSn and Au<sub>5</sub>Sn. However, this study has demonstrated that the as-cast Au–20Sn eutectic

alloy has superplasticity during hot compression when the temperature is above 200 °C, suggesting that the hot plastic process may have the potential to fabricate Au–20Sn foil. Among the metal forming processes, hot rolling is an effective hot plastic process that can simultaneously realize the size and surface-quality requirements. However, parameters such as the temperature, rolling speed, and pass reduction available for hot rolling on Au–20Sn are not clear. The trial-and-error method is not appropriate to explore these parameters because of the extremely expensive raw materials.

In fact, the parameters needed in hot rolling can be approximately summarized by the present results of compressive experiments. Since strain rate during rolling can be calculated, such a parameter can help us establish a relationship between the compression and rolling processes. ZHAO and TIE [37] proposed a calculation method named the “exact contact arc” based on the evaluation and improvement of previous methods, where the strain rate ( $\dot{\varepsilon}$ ) of a metal alloy during rolling can be expressed by [37]

$$\dot{\varepsilon} = \frac{2\nu h_1}{\theta(D+h_1)} \left[ \ln \frac{h_1 \cos \theta}{h_0} - \varepsilon \left( \frac{D}{h_1} + 1 \right) \right] \quad (1)$$

$$\varepsilon = \frac{h_0 - h_1}{h_0} \quad (2)$$

where  $v$  is the linear rolling speed,  $h_0$  and  $h_1$  are the sample thicknesses before and after a rolling pass,  $\varepsilon$  is the pass reduction,  $D$  is the diameter of the rollers, and  $\theta$  is the maximum contact angle between the sample and the rollers. For an Au–20Sn alloy during rolling, the initial sample thickness  $h_0$ , the diameter of rollers  $D$ , and the maximum contact angle  $\theta$  are known. Therefore, when a strain rate is given, the equation will express a relationship between the  $v$  and  $h_1$ . Thus, the relationship between the linear rolling speed ( $v$ ) and the pass reduction ( $\varepsilon$ ) can be determined conditionally.

Based on the above concept, we performed a tentative hot rolling experiment on an as-cast Au–20Sn alloy. First, the strain rate and the rolling temperature were determined. Regarding the rolling process, the higher the strain rate is, the higher the production efficiency. Clearly, the strain rate of  $0.001 \text{ s}^{-1}$  is too low and the strain rate can be preliminarily set in the strain rate range of  $0.1\text{--}0.6 \text{ s}^{-1}$  because the Au–20Sn alloy still possesses superplasticity in this strain rate range. Considering that the samples deformed at  $200 \text{ }^\circ\text{C}$  show rough surfaces at  $0.1 \text{ s}^{-1}$  and show edge cracks at  $0.6 \text{ s}^{-1}$ , temperatures above  $200 \text{ }^\circ\text{C}$  are suitable for the rolling process. To further discuss the temperature, the true flow stresses of the Au–20Sn alloy during hot compression at the strain rates of  $0.1 \text{ s}^{-1}$  and  $0.6 \text{ s}^{-1}$  are listed in Table 1. It shows that the softening effect of the alloy at  $220 \text{ }^\circ\text{C}$  is substantial, and the softening efficiency will be reduced when the deformation temperature is increased to  $240 \text{ }^\circ\text{C}$ . Additionally, after being compressed at  $240 \text{ }^\circ\text{C}$ , the samples are easily stuck to the compressive equipment. This indicates that

the temperature of  $240 \text{ }^\circ\text{C}$  is a slightly high for plastic forming since the temperature has reached  $0.86T_m$  of the Au–20Sn alloy. Hence,  $220 \text{ }^\circ\text{C}$  should be an appropriate and economic temperature for the forming of Au–20Sn alloy in the hot rolling process.

Figure 14(a) shows the tentative hot rolling experiment. An as-cast Au–20Sn ingot with dimensions of  $20 \text{ mm}$  (length)  $\times$   $20 \text{ mm}$  (width)  $\times$   $4 \text{ mm}$  (thickness) was prepared as the rolling sample. The rolling strain rate and temperature were set to be  $0.1 \text{ s}^{-1}$  and  $220 \text{ }^\circ\text{C}$ . Based on the above equations, the relationship between the rolling reduction ( $\varepsilon$ ) and the linear speed can be calculated, as listed in Table 2. In view of the production efficiency, a linear speed of  $1 \text{ m/min}$  was selected, and the allowable pass reduction corresponds to  $\sim 15\%$  at the rolling strain rate of  $0.1 \text{ s}^{-1}$ . The pass reduction was set to be  $15\%\text{--}20\%$  in the actual rolling experiment, because the strain rate of  $0.1 \text{ s}^{-1}$  is relatively conservative since the alloy can also be successfully compressed at a higher strain rate of  $0.6 \text{ s}^{-1}$  at  $220 \text{ }^\circ\text{C}$ . Prudently, based on these parameters, the as-cast Au–20Sn ingot was successfully deformed to prepare a foil with a thickness of  $\sim 50 \mu\text{m}$ , as shown in Fig. 14(b). The experiment proves the determination of rolling parameters by showing the results that obtained from the hot compression process are credible.

There are still some issues that can be focused to improve the rollability of the alloy, and thus to enhance the rolling productivity. For the Au–20Sn alloy with a lamellar structure subjected to hot compression, it is clear that the lamellar growth direction has a significant influence on the spheroidization rate. Therefore, regulating the lamellar growth direction during casting to introduce

**Table 1** Flow stress of Au–20Sn alloy during compression under different deformation conditions

Condition	$\sigma_{0.1 \text{ s}^{-1}}/\text{MPa}$			$\sigma_{0.6 \text{ s}^{-1}}/\text{MPa}$		
	$\varepsilon=60\%$	$\varepsilon=120\%$	$\varepsilon=200\%$	$\varepsilon=60\%$	$\varepsilon=120\%$	$\varepsilon=200\%$
$200 \text{ }^\circ\text{C}$	192.3	224.7	227.6	201.5	200.0	211.8
$220 \text{ }^\circ\text{C}$	135.6	165.8	198.2	144.5	135.6	169.1
$240 \text{ }^\circ\text{C}$	108.9	139.3	178.0	114.6	113.2	145.6
$A_1$	−56.7	−58.9	−33.6	−57.0	−64.4	−42.7
$A_2$	−26.7	−26.5	−18.2	−29.9	−22.4	−23.5
avg $A_2$ /avg $A_1$		48.8%			47.4%	

$$A_1 = \sigma_{220 \text{ }^\circ\text{C}} - \sigma_{200 \text{ }^\circ\text{C}}; A_2 = \sigma_{240 \text{ }^\circ\text{C}} - \sigma_{220 \text{ }^\circ\text{C}}$$

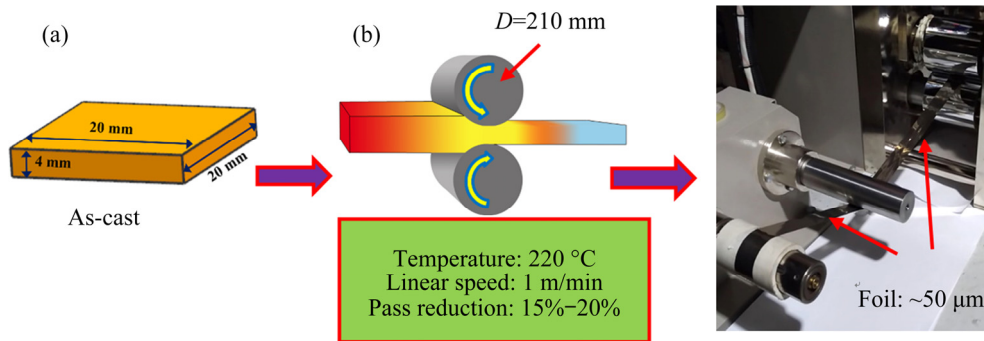


**Fig. 14** Hot rolling performed on as-cast Au–20Sn alloy: (a) Ingot prepared by rolling process; (b) Rolling parameters and Au–20Sn foil successfully fabricated by hot rolling process

**Table 2** Relationships between pass reduction and linear speed of Au–20Sn alloy rolled at 220 °C and  $0.1 \text{ s}^{-1}$

Pass reduction, $\varepsilon/\%$	Linear speed, $v/(\text{m} \cdot \text{min}^{-1})$
5	1.74
7.5	1.43
10	1.24
15	1.02
20	0.89
25	0.78
30	0.72

a great fraction of vertical lamellae may be an effective method that can promote the spheroidization rate and improve the deformability of the alloy. Additionally, because the microstructural spheroidization process is initiated from the shear instability regions, appropriately increasing the shear stress during rolling (such as employing differential speed rolling) may be another potential way. On one hand, a higher shear stress can contribute to promoting the spheroidization rate. On the other hand, the introduction of shear stress can refine the grain size of the recrystallized microstructure. A fine equiaxed microstructure can effectively promote GB sliding and migration, and thus improve the deformability of the alloy during hot rolling process.

## 5 Conclusions

(1) The multilayered Au–20Sn eutectic alloy possessed compressive superplasticity in a strain rate range of  $0.001\text{--}0.6 \text{ s}^{-1}$  when the deformation temperature increased to 200 °C. To acquire a better surface-quality after compressing the alloy in a high

strain rate range of  $0.1\text{--}0.6 \text{ s}^{-1}$ , the deformation temperature should be increased to 220 °C to prevent the formation of rough surfaces and edge cracks.

(2) Microstructural spheroidization occurred extensively in the nanolayered colonies of the Au–20Sn alloy during hot compression. It initiated from the plastic instability regions with severe shear and gradually spread in the lamellar colonies. Moreover, the spheroidization rate was sensitive to the initial lamellar growth direction, and spheroidization was preferentially activated in the vertical lamellae with a growth direction parallel to the compressive direction.

(3) Continuous dynamic recrystallization was the mechanism of microstructural spheroidization in the multilayers during hot compression. The primary deformation mechanisms for the AuSn and Au<sub>5</sub>Sn layers were  $\{10\bar{1}0\}\langle 11\bar{2}0 \rangle$  prismatic slip and  $(0001)\langle 11\bar{2}0 \rangle$  basal slip, respectively.

(4) After the spheroidization process, strain accumulation in terms of lattice dislocations in the equiaxed phases was significantly weakened compared to that in the lamellar phases. The deformation mechanism was substantially replaced by grain boundary sliding and migration.

(5) Based on the findings from the hot compression process, a hot rolling experiment was performed on an as-cast Au–20Sn alloy and a foil with a thickness of  $\sim 50 \mu\text{m}$  was successfully prepared.

(6) The present study can promote the development of Au–20Sn alloy foils, as well as provide insights into the hot deformation behavior and microstructure evolution of multilayered eutectic alloys.

## Acknowledgments

The authors are grateful for the financial supports from the National Natural Science Foundation of China (Nos. U1502272, 51901204), and the Precious Metal Materials Genome Engineering in Yunnan Province, China (Nos. 2019ZE001, 202002AB080001).

## References

- [1] CHENG Shun-feng, HUANG Chien-ming, PECHT M. A review of lead-free solders for electronics applications [J]. *Microelectronics Reliability*, 2017, 75: 77–95.
- [2] WEI Xiao-feng, ZHANG Yu-kun, WANG Ri-chu, FENG Yan. Microstructural evolution and shear strength of AuSn20/Ni single lap solder joints [J]. *Microelectronics Reliability*, 2013, 53: 748–754.
- [3] RAUTIAINEN A, XU Hong-bo, ÖSTERLUND E, LI Jue, VUORINEN V, KROCKEL M. Microstructural characterization and mechanical performance of wafer-level SLID bonded Au–Sn and Cu–Sn seal rings for MEMS encapsulation [J]. *Journal of Electronic Materials*, 2015, 44: 4533–4548.
- [4] TUNTHAWIROON P, KANLAYASIRI K. Effects of Ag contents in Sn–xAg lead-free solders on microstructure, corrosion behavior and interfacial reaction with Cu substrate [J]. *Transactions of Nonferrous Metals Society of China*, 2019, 22: 1696–1704.
- [5] WEI Xiu-qin, HUANG Hui-zhen, ZHOU Liang, ZHANG Meng, LIU Xiao-dong. On the advantages of using a hypoeutectic Sn–Zn as lead-free solder material [J]. *Materials Letter*, 2007, 61: 655–658.
- [6] MOUSAVI T, AKSOY C, GROVENOR C, SPELLER S. Phase evolution of superconducting Sn–In–Bi solder alloys [J]. *IEEE Transactions on Applied Superconductivity*, 2016, 26(3): 1-1.
- [7] JING Hong-qi, NI Yu-xi, LIU Qi-kun, ZHONG Li, KONG Jin-xia, WANG Xin, LIU Su-ping, MA Xiao-yu. Performance of semiconductor laser devices packaged by different AuSn solder composition [J]. *Chinese Journal of Luminescence*, 2018, 39: 850–854.
- [8] ZHU Z, LI C, LIAO L, LIU C, KAO C. Au–Sn bonding material for the assembly of power integrated circuit module [J]. *Journal of Alloys and Compounds*, 2016, 671: 340–345.
- [9] TAN Qing-biao, DENG Chao, MAO Yong, HE Guo. Evolution of primary phases and high-temperature compressive behaviors of as-cast AuSn20 alloys prepared by different solidification pathways [J]. *Gold Bulletin*, 2011, 44: 27–35.
- [10] MATIJASEVIC G S, LEE C C, WANG C Y. Au–Sn alloy phase diagram and properties related to its use as a bonding medium [J]. *Thin Solid Films*, 1993, 223: 276–287.
- [11] LIU Sheng-fa, CHEN Chen, XIONG Jie-ran, XIONG Wen-yong, HU Zhe-bin, HUANG Shang-yu. Research progress in preparation technology of AuSn20 eutectic alloy solder [J]. *Special Casting and Nonferrous Alloys*, 2017, 39: 952–956.
- [12] TANG Wen-ming, HE An-qiang, LIU Qi, IVEY D G. Room temperature interfacial reactions in electrodeposited Au/Sn couples [J]. *Acta Materialia*, 2008, 56: 5818–5827.
- [13] CIULIK J, NOTIS M R. The AuSn phase diagram [J]. *Journal of Alloys and Compounds*, 1993, 191: 71–78.
- [14] YANG Jiang-rong. Study on microstructure evolution of Au–Sn eutectic alloy during hot rolling [M]. Kunming: Yunnan University, 2018. (in Chinese)
- [15] XIE Ji-yang, LU Sheng-lai, DU Ya-nan, HU Wan-biao, MAO Yong. Microstructural evolution and orientation-correlated origin of the coarsening behaviors in Au–Sn eutectic alloys [J]. *Journal of Alloys and Compounds*, 2019, 806: 1285–1291.
- [16] RODRIGUEZ R I, IBITAYO D, QUINTERO P O. Thermal stability characterization of the Au–Sn bonding for high-temperature applications [J]. *IEEE Transactions on Components, Packaging, and Manufacturing Technology*, 2013, 3: 549–557.
- [17] HUMPHREYS F J. Review grain and subgrain characterisation by electron backscatter diffraction [J]. *Journal of Materials Science*, 2001, 36: 3833–3854.
- [18] ASHTIANI H R, SHAHSAVARI P. Constitutive modeling of flow behavior of precipitation-hardened AA7022-T6 aluminum alloy at elevated temperature [J]. *Transactions of Nonferrous Metals Society of China*, 2020, 30: 2927–2940.
- [19] WANG S J, LIU G S, XIE D Y, LEI Q, RAMAKRISHNAN B, MAZUMDER J, WANG Jian, MISRA A. Plasticity of laser-processed nanoscale Al–Al<sub>2</sub>Cu eutectic alloy [J]. *Acta Materialia*, 2018, 156: 52–63.
- [20] CHEN Ke, WU Jie-qiong, SHI Hui, CHEN Xing-fang, SHEN Zhi, ZHANG Mei, ZHANG Lan-ting, SHAN Ai-dang. Transition of deformation behavior and its related microstructure evolution in Nimonic 80A under hot-to-warm working [J]. *Materials Characterization*, 2015, 106: 175–184.
- [21] JIANG Ju-fu, XIAO Guan-fei, WANG Ying, LIU Ying-ze. ZHANG Ying. High temperature deformation behavior and microstructure evolution of wrought nickel-based superalloy GH4037 in solid and semi-solid states [J]. *Transactions of Nonferrous Metals Society of China* 2020, 30: 710–726.
- [22] SANDLBES S, ZAEFFERER S, SCHESTAKOW I, YI S, GONZALEZ R. On the role of non-basal deformation mechanisms for the ductility of Mg and Mg–Y alloys [J]. *Acta Materialia*, 2011, 59: 429–439.
- [23] SINGH J, KIM M S, LEE S E, KIM E Y, KANG J H, PARK J H, KIM J J, HOI S H. Heterogeneity in deformation and twinning behaviors through the thickness direction in E-form Mg alloy sheets during an Erichsen test [J]. *Materials Science and Engineering A*, 2018, 729: 370–384.
- [24] WEI Yu-jie, BOWER A F, GAO Hua-jian. Enhanced strain-rate sensitivity in fcc nanocrystals due to grain-boundary diffusion and sliding [J]. *Acta Materialia*, 2008, 56: 1741–1752.
- [25] BOBYLEV S V, MORIZOV N F, OVIDKO I A. Cooperative grain boundary sliding and migration process in nanocrystalline solids [J]. *Physical Review Letters*, 2010, 105: 055504.
- [26] FAN Rong-lei, WU Yong, CHEN Ming-he, XIE Lan-sheng. Relationship among microstructure, mechanical properties

- and texture of TA32 titanium alloy sheets during hot tensile deformation [J]. Transactions of Nonferrous Metals Society of China, 2020, 30: 928–943.
- [27] CHUN Y, DAVIES C. Investigation of prism  $\langle a \rangle$  slip in warm-rolled AZ31 alloy [J]. Metallurgical and Materials Transactions A, 2011, 42: 4113–4125.
- [28] HE Jun-jie, MAO Yong, LU Sheng-lai, XIONG Kai, ZHANG Shun-meng, JIANG Bin, PAN Fu-sheng. Texture optimization on Mg sheets by preparing soft orientations of extension twinning for rolling [J]. Materials Science and Engineering A, 2019, 760: 174–185.
- [29] LI Rui-hong, PAN Fu-sheng, JIANG Bin, DONG Han-wu, YANG Qing-shan. Effect of Li addition on the mechanical behavior and texture of the as-extruded AZ31 magnesium alloy [J]. Materials Science and Engineering A, 2013, 562: 33–38.
- [30] HAUSER F E, LANDON P R, DORN J E. Deformation and fracture of alpha solid solutions of lithium in magnesium [J]. ASM-Trans, 1958, 50: 856–883.
- [31] HE Jun-jie, MAO Yong, FU Ying-jie, JIANG Bin, XIONG Kai, ZHANG Shun-meng, PAN Fu-sheng. Improving the room-temperature formability of Mg–3Al–1Zn alloy sheet by introducing an orthogonal four-peak texture [J]. Journal of Alloys and Compounds, 2019, 797: 443–455.
- [32] BEDNARCZYK W, KAWALKO J, WATROBA M, GAO N, STARINK M J, BALA P, LANGDON T G. Microstructure and mechanical properties of a Zn–0.5Cu alloy processed by high-pressure torsion [J]. Materials Science and Engineering A, 2020, 776: 139047.
- [33] TENCKHOFF E. The development of the deformation texture in zirconium during rolling in sequential passes [J]. Metallurgical Transactions A, 1978, 9: 1401–1412.
- [34] WAGNER F, BOZZOLO N, LANDUYT O V, GROSDIDIER T. Evolution of recrystallisation texture and microstructure in low alloyed titanium sheets [J]. Acta Materialia, 2002, 50: 1245–1259.
- [35] SUH B C, KIM J H, BAE J H, JI H H, SHIM M S, KIM N J. Effect of Sn addition on the microstructure and deformation behavior of Mg–3Al alloy [J]. Acta Materialia, 2017, 124: 268–279.
- [36] ZHOU Zi-qiang, YUE Xue-lan, HUO Deng-ping. Influence of grain boundary structure on migration of grain boundary [J]. Ordnance Material Science and Engineering, 1998, 21: 3–8.
- [37] ZHAO De-wen, TIE Wei-lin. A precise method of calculating the parameter  $\bar{\epsilon}$  — The mean strain rate in rolling [J]. Journal of Applied Sciences, 1995, 13: 103–108.

## Au–Sn 共晶多层材料的热变形行为及组织演化

毛 勇<sup>1,2,3</sup>, 祝丹丽<sup>1,3</sup>, 何俊杰<sup>1,2,3</sup>, 邓 超<sup>4</sup>, 孙莹洁<sup>1,3</sup>, 薛广杰<sup>1,3</sup>, 余恒飞<sup>1,3</sup>, 王 琛<sup>1,3</sup>

1. 云南大学 材料与能源学院, 昆明 650091;
2. 云南大学 物理与天文学院, 昆明 650091;
3. 云南大学 材料基因工程研究中心, 昆明 650091;
4. 重庆大学 材料科学与工程学院, 重庆 400045

**摘 要:** 研究多层组织 Au–20Sn 共晶合金在热压缩过程中的变形行为及组织演变。结果表明, 合金层状组织在热变形中发生塑性失稳, 球化行为会在失稳区域启动并逐步在层片团内蔓延。组织球化优先发生于层片生长方向与压缩方向平行的层片团内部, 其球化机制为 AuSn/Au<sub>5</sub>Sn 层片内部位错演化牵动的不连续动态再结晶。球化完成后, 两等轴相内部的应变积累能力均弱化, 变形机制由位错滑移转变为晶界滑动和迁移。基于上述研究, 设计 Au–20Sn 铸态合金的热轧成形实验, 并成功制备出厚度为~50 μm 的箔材。本研究不仅能促进 Au–20Sn 箔材材料的发展应用, 也将为多层组织合金的变形及组织演变提供理论参考。

**关键词:** Au–20Sn 共晶合金; 金属间化合物; 热压缩; 多层组织; 变形; 球化

(Edited by Xiang-qun LI)